

Repurposing Geometric Foundation Models for Multi-view Diffusion

Wooseok Jang¹, Seonghu Jeon¹, Jisang Han¹, Jinhyeok Choi¹,
Minkyung Kwon¹, Seungryong Kim¹, Saining Xie², and Sainan Liu³

¹KAIST AI ²New York University ³Intel Labs
<https://cvlab-kaist.github.io/GLD>

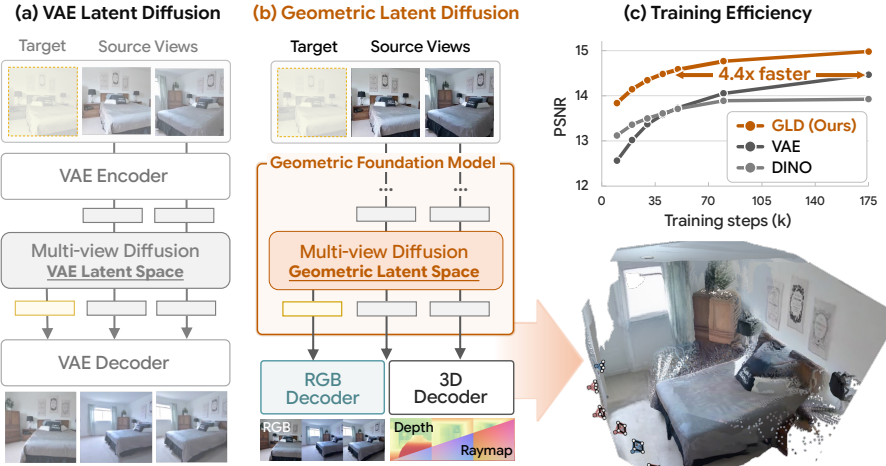


Fig. 1: (a) Prior multi-view diffusion operates in a view-independent VAE [36] latent space. (b) **Geometric Latent Diffusion (GLD)** instead diffuses in a geometrically consistent feature space of geometric foundation models [26, 47], enabling both RGB and geometry decoding. (c) GLD converges $4.4\times$ faster than VAE [36] and DINO [56].

Abstract. While recent advances in the latent space have driven substantial progress in single-image generation, the optimal latent space for novel view synthesis (NVS) remains largely unexplored. In particular, NVS requires geometrically consistent generation across viewpoints, but existing approaches typically operate in a view-independent VAE latent space. In this paper, we propose **Geometric Latent Diffusion (GLD)**, a framework that repurposes a geometrically consistent feature space of geometric foundation models as the latent space for multi-view diffusion. We show that the features of the geometric foundation model not only support high-fidelity RGB reconstruction but also encode strong cross-view geometric correspondences, providing a well-suited latent space for NVS. Through experiments, GLD outperforms both VAE and RAE on 2D image quality and 3D consistency metrics, accelerating training by more than $4.4\times$ compared to the VAE latent space. Notably, GLD remains competitive with state-of-the-art methods that leverage large-scale text-to-image pretraining, despite training its diffusion model from scratch without such generative pretraining.

1 Introduction

Diffusion models [14, 44] have become the dominant framework for image synthesis. Transitioning from pixel space to the variational auto-encoder’s (VAE) latent space [23, 33, 36], and further to semantically structured representations [41, 45, 56], has shown that the latent space significantly influences generation quality and training efficiency. However, these insights have been drawn exclusively from 2D image generation, and the design of effective latent spaces for **geometry-aware generation tasks** remains largely unexplored.

Novel view synthesis (NVS), which predicts unseen viewpoints consistent with an underlying 3D scene [21, 40], is a representative geometry-aware generation task. Unlike single-image generation, this task requires maintaining coherent spatial structure across views and geometrically plausible completion of occluded regions. While early generative approaches [12, 42] have demonstrated photorealistic image quality, they often prioritize appearance over geometric consistency, leading to geometrically inconsistent outputs. To address this, recent diffusion-based NVS methods often leverage external geometry conditioning, such as depth-based warping [4, 21, 40, 53]. However, these approaches still rely on latent spaces originally designed for single-image synthesis models, such as the 2D VAEs [36]. This raises a fundamental question: **can we leverage a latent space in which geometric structure is already encoded, rather than injecting or supervising it externally?**

In this work, we propose **Geometric Latent Diffusion (GLD)** that utilizes the feature space of geometric foundation models [26, 47, 51] such as VGGT [47] or Depth Anything 3 [26] as a **latent space for multi-view diffusion models**. We first show that the features of a geometric foundation model support high-fidelity, view-consistent RGB reconstruction, enabling the diffusion process to operate directly on geometry-aware representations for NVS. By training in this geometry-informed latent space, GLD leverages the rich geometric structure, which provides the necessary grounding for generating view-consistent images. Furthermore, since our framework operates natively on the geometric foundation model’s features, synthesized latents can be directly decoded into geometric predictions (*e.g.*, depth maps and camera poses) without additional training.

In addition, geometric foundation models typically produce a hierarchy of multi-level features to reconstruct 3D geometries. To ensure computational efficiency, rather than diffusing the entire multi-level features, we identify an optimal boundary layer level for explicit synthesis. Deeper-layer features beyond this boundary are naturally derived by propagating through the frozen backbone, while shallower features are generated via a cascaded scheme to ensure cross-level alignment.

Through extensive experiments on both in-domain and zero-shot benchmarks, GLD achieves superior pixel-level fidelity and cross-view 3D consistency compared with VAE [36] and RAE [56] baselines, accelerating training convergence by over $4.4\times$. Although our diffusion model is trained from scratch on small datasets, GLD remains competitive with state-of-the-art methods [4, 12, 22, 24, 30], fine-tuned from large-scale text-to-image models. Moreover, zero-shot depth

and 3D point clouds decoded from synthesized latents exhibit strong global consistency. These results validate that our GLD framework effectively integrates generative modeling with a geometry-informed latent representation.

2 Related Work

Novel View Synthesis with Diffusion Models. Classical geometry-based approaches to novel view synthesis [17, 31] produce photorealistic renderings but require dense multi-view captures and costly per-scene optimization. Recent multi-view diffusion models [4, 12, 19, 21, 30, 40, 53, 57] alleviate these constraints by leveraging generative priors to synthesize novel views from sparse inputs. However, these methods operate in pixel or VAE latent spaces that lack cross-view geometric structure, placing a substantial burden on the model to implicitly discover geometric correspondences [22]. We instead train multi-view diffusion models in a latent space that already encodes this structure.

Latent Spaces for Diffusion Models. Latent diffusion models (LDMs) [36] have advanced image synthesis by operating in a compressed VAE [18] latent space, but it lacks rich structural priors. RAE [45, 56] and SVG [41] show that frozen semantic encoders [32, 43, 46] can be paired with lightweight decoders for high-fidelity reconstruction, and that diffusing in this semantic space yields faster convergence and improved generation quality. However, these advances target single-image generation, leaving open the question of how to design latent spaces for geometry-aware generation tasks. Recent works address this by training dedicated autoencoders that jointly encode appearance and geometry, for single-image [20] and text-to-3D [52] generation. Our work instead repurposes the feature space of an existing geometric foundation model [26] as the latent space for diffusion, providing the model with cross-view geometric priors.

Geometric Foundation Models. Geometric foundation models have introduced a paradigm shift in 3D vision, moving from optimization-based feature matching [38] to purely feed-forward scene understanding. Building on the pairwise formulation of DUST3R [49], recent models [16, 26, 47, 51] have enabled feed-forward dense 3D reconstruction from arbitrary unposed views, jointly predicting camera parameters and depth maps. While recent analyses reveal that the internal representations of these networks encode strong geometric correspondences [13], their utility has been largely limited to discriminative tasks. We bridge this gap by showing that the feature space of a geometric foundation model [26] can serve as an effective latent space for novel view synthesis.

3 Preliminaries

Representation Autoencoder. Representation Autoencoder (RAE) [45, 56] replaces the conventional VAE [18] in latent diffusion [36] with a pretrained, frozen vision encoder [32, 46] $\mathcal{E}(\cdot)$ and a trainable decoder $\mathcal{D}(\cdot)$, directly adopting the encoder’s feature space as the diffusion latent space.

Specifically, the decoder is trained to reconstruct RGB images from features in this representation space, showing that these features are not only semantically rich but also sufficient for high-fidelity reconstruction. Formally, given a single-view image $\mathcal{I} \in \mathbb{R}^{H \times W \times 3}$, where H and W denote the height and width, respectively, the encoder extracts a tokenized feature representation

$$\mathbf{F} = \mathcal{E}(\mathcal{I}) \in \mathbb{R}^{T \times C}, \quad (1)$$

where T is the token sequence length and C is the channel dimension. RAE further shows that diffusion models can be trained directly in this representation space, yielding faster convergence and stronger generative performance than training in conventional VAE latent spaces [18]. During generation, the diffusion model synthesizes $\tilde{\mathbf{F}}$, and the synthesized image $\tilde{\mathcal{I}}$ is then obtained by decoding the synthesized feature: $\tilde{\mathcal{I}} = \mathcal{D}(\tilde{\mathbf{F}})$.

Geometric Foundation Models. Recent foundation models for geometry [26, 47, 51] typically consist of a Vision Transformer (ViT) [8] encoder $\mathcal{E}_{\text{geo}}(\cdot)$ and a DPT-based geometric decoder $\mathcal{D}_{\text{geo}}(\cdot)$. To process multi-view inputs, these architectures often incorporate 3D attention in addition to standard intra-image self-attention, which enables joint reasoning across multiple frames. Given multi-view images $\mathbf{I} \in \mathbb{R}^{V \times H \times W \times 3}$, where V is the number of input views, the encoder extracts multi-view feature sequences at L levels (often $L = 4$):

$$\{\mathbf{F}_l\}_{l=0}^{L-1} = \mathcal{E}_{\text{geo}}(\mathbf{I}), \quad (2)$$

where $\mathbf{F}_l \in \mathbb{R}^{V \times T \times C}$ denotes the multi-view feature sequence at level l , with T the token sequence length and C the channel dimension. The geometric decoder then aggregates these multi-level features to produce dense geometric predictions, such as depth or camera parameters:

$$\mathbf{G} = \mathcal{D}_{\text{geo}}(\{\mathbf{F}_l\}_{l=0}^{L-1}), \quad (3)$$

where \mathbf{G} denotes a set of geometric predictions for each input view.

4 Method

4.1 Overview

Our goal is to harness the feature space of geometric foundation models [26, 47, 51] as the latent space for multi-view diffusion, enabling high-fidelity novel view synthesis (NVS). Specifically, we adopt the Depth Anything 3 (DA3) [26] as our primary backbone, which extracts features across $L = 4$ intermediate levels. We also explore VGGT [47] as an additional backbone in Appendix C.1. Given a set of N source images $\mathbf{I}^{\text{src}} \in \mathbb{R}^{N \times H \times W \times 3}$ with camera poses \mathbf{P}^{src} , and M target camera poses \mathbf{P}^{tgt} , we seek to synthesize the corresponding target views $\tilde{\mathbf{I}}^{\text{tgt}} \in \mathbb{R}^{M \times H \times W \times 3}$. Rather than operating directly in pixel space or VAE space [36], our framework generates multi-view, multi-level features from geometric foundation models [26, 47, 51], which are subsequently decoded into the target views.

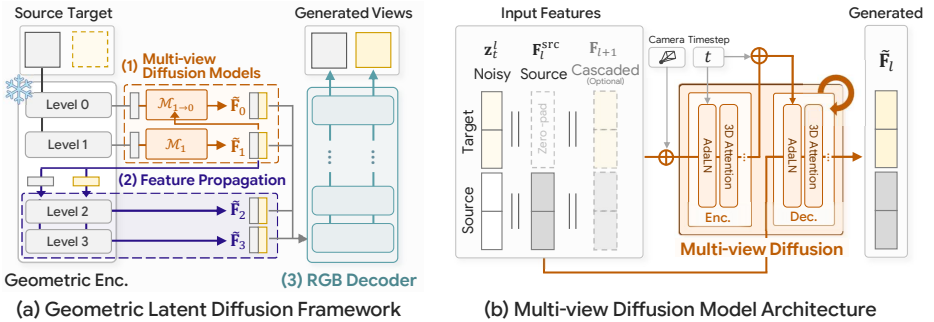


Fig. 2: Overview of the proposed framework. (a) Our NVS framework consists of three stages: (1) **multi-view diffusion models** synthesize features up to boundary layer $k=1$ via cascaded generation, (2) **feature propagation** derives deeper features through the frozen DA3 encoder, and (3) **the RGB decoder** maps the full multi-level features to target views. (b) The detailed architecture of a multi-view diffusion model.

Because the geometric foundation model’s 3D attention jointly encodes source and target views, the resulting features are inherently coupled. We therefore generate both source and target features across all levels, denoted as $\{\tilde{\mathbf{F}}_l^{\text{src}}\}_{l=0}^{L-1}$ with $\tilde{\mathbf{F}}_l^{\text{src}} \in \mathbb{R}^{N \times T \times C}$, and $\{\tilde{\mathbf{F}}_l^{\text{tgt}}\}_{l=0}^{L-1}$ with $\tilde{\mathbf{F}}_l^{\text{tgt}} \in \mathbb{R}^{M \times T \times C}$. At each level l , the joint feature $\tilde{\mathbf{F}}_l \in \mathbb{R}^{(N+M) \times T \times C}$ is formed by concatenating the source and target features along the view dimension, yielding $\tilde{\mathbf{F}}_l = [\tilde{\mathbf{F}}_l^{\text{src}}, \tilde{\mathbf{F}}_l^{\text{tgt}}]$ with concatenation operator $[\cdot, \cdot]$. Finally, a dedicated RGB decoder $\mathcal{D}_{\text{rgb}}(\cdot)$ maps the complete synthesized feature set back to the pixel space to render the target views via $\tilde{\mathbf{I}}^{\text{tgt}} = \mathcal{D}_{\text{rgb}}(\{\tilde{\mathbf{F}}_l^{\text{tgt}}\}_{l=0}^{L-1})$. The target geometry $\tilde{\mathbf{G}}^{\text{tgt}}$ is also decoded such that $\tilde{\mathbf{G}}^{\text{tgt}} = \mathcal{D}_{\text{geo}}(\{\tilde{\mathbf{F}}_l^{\text{tgt}}\}_{l=0}^{L-1})$.

To this end, as illustrated in Fig. 2, **Geometric Latent Diffusion (GLD)** framework employs a three-stage pipeline. First, § 4.2 validates the reconstruction capacity of the geometric feature space by training $\mathcal{D}_{\text{rgb}}(\cdot)$ to decode multi-level features into RGB images. Second, to avoid the substantial cost of diffusing all L feature levels, § 4.3 identifies the optimal boundary layer k . Since deeper features can be obtained by propagating the boundary feature $\tilde{\mathbf{F}}_k$ through $\mathcal{E}_{\text{geo}}(\cdot)$, we only require explicit synthesis up to this boundary feature. Finally, § 4.4 employs a cascaded scheme to synthesize shallower features from $\tilde{\mathbf{F}}_k$ to ensure cross-level alignment.

4.2 Validating the Reconstruction Capability of Geometric Features

To validate the suitability of DA3’s feature space for generative modeling, we first verify that its features can be decoded into high-fidelity images. We train a ViT-based decoder $\mathcal{D}_{\text{rgb}}(\cdot)$ to reconstruct RGB images from the multi-level features $\{\mathbf{F}_l\}_{l=0}^{L-1}$ extracted by the frozen encoder $\mathcal{E}_{\text{geo}}(\cdot)$. To ensure $\mathcal{D}_{\text{rgb}}(\cdot)$ effectively leverages the full signal, we introduce a level-wise dropout strategy during training. By randomly masking individual levels in $\{\mathbf{F}_l\}_{l=0}^{L-1}$, we force the decoder to reconstruct from partial inputs, improving its robustness.



Fig. 3: Reconstruction Results. We visualize the reconstructed images from $\mathcal{D}_{\text{rgb}}(\cdot)$.

As shown in Tab. 1 and Fig. 3, $\mathcal{D}_{\text{rgb}}(\cdot)$ successfully recovers the input images with high fidelity while preserving fine-grained details. These results show that the DA3 feature space is suitable as the latent space for our diffusion process. Further details and comparison with other baselines are available in § 5.4.

4.3 Multi-view Diffusion and Determining the Boundary Layer

While the DA3 feature space provides a sufficiently expressive latent for high-fidelity image reconstruction, explicitly synthesizing the full multi-level set $\{\mathbf{F}_l\}_{l=0}^3$ is computationally prohibitive. Since deeper features ($l > k$) can be deterministically derived by propagating a shallower feature $\tilde{\mathbf{F}}_k$ through the frozen layers of \mathcal{E}_{geo} , we only require explicit synthesis up to an optimal boundary k . To identify this boundary, we first train four independent diffusion models $\{\mathcal{M}_l\}_{l=0}^3$, each dedicated to synthesizing the target feature at a specific level l . We then perform a comparative evaluation by varying the synthesis boundary $k \in \{0, 1, 2, 3\}$ to identify the shallowest boundary sufficient for high-quality NVS.

Multi-view Diffusion Architecture and Training. We adopt the DiT^{DH} [48] architecture from RAE [56] and train it with a flow-matching objective [28] to synthesize the joint feature map $\tilde{\mathbf{F}}_l$ for all $V = N + M$ views. As illustrated in Fig. 2, we incorporate 3D self-attention [12] with PRoPE [25] and condition on Plücker ray embeddings to enforce geometric consistency across views.

Each model \mathcal{M}_l is conditioned on the source-only features $\mathbf{F}_l^{\text{src}}$, extracted by the frozen DA3 encoder from the N source images alone, by concatenating them with the noisy latent \mathbf{z}_t along the channel dimension. Note that $\mathbf{F}_l^{\text{src}}$ is extracted without access to target views, whereas the source portion of the full joint feature \mathbf{F}_l is influenced by 3D attention over all V views. Because the decoder and downstream stages require features from all views, we design the model to jointly generate \mathbf{F}_l rather than generate only the target views.

Boundary Layer Evaluation. To identify the optimal boundary, we assess how each level k contributes to the generation by providing the decoder \mathcal{D}_{rgb} with a complete multi-level set $\{\tilde{\mathbf{F}}_l\}_{l=0}^3$. For a given boundary k , we explicitly synthesize the features up to that level ($l \leq k$), $\{\tilde{\mathbf{F}}_l\}_{l=0}^k$, using the corresponding set of independently trained models $\{\mathcal{M}_l\}_{l=0}^k$. The remaining deeper levels ($l > k$) are then deterministically derived by passing $\tilde{\mathbf{F}}_k$ through the frozen layers of $\mathcal{E}_{\text{geo}}(\cdot)$.

As shown in Tab. 2, synthesizing up to level 1 achieves superior NVS performance. Shifting the boundary from level 0 to level 1 improves both RGB

Table 1: Reconstruction Fidelity. We evaluate our RGB decoder on 4,000 samples from the Re10K [58] test set.

Metrics	Decoder (\mathcal{D}_{rgb})
PSNR \uparrow	35.41
SSIM \uparrow	0.960
LPIPS \downarrow	0.019

Table 2: Boundary Selection. We evaluate NVS performance by varying the synthesis boundary k . Explicitly synthesizing up to level $l = 1$ (Boundary $k = 1$) using \mathcal{M}_0 and \mathcal{M}_1 provides the best performance across all metrics.

Synthesis Configuration		RGB Metrics			Depth Metrics		
Boundary k	Models $\{\mathcal{M}_l\}_{l=0}^k$	PSNR \uparrow	SSIM \uparrow	LPIPS \downarrow	AbsRel \downarrow	RMSE \downarrow	$\delta < 1.25 \uparrow$
$k = 0$	$\{\mathcal{M}_0\}$	12.55	0.323	0.579	0.267	0.400	0.641
$k = 1$	$\{\mathcal{M}_0, \mathcal{M}_1\}$	13.61	0.366	0.555	0.191	0.311	0.744
$k = 2$	$\{\mathcal{M}_0, \mathcal{M}_1, \mathcal{M}_2\}$	13.35	0.355	0.566	0.254	0.393	0.659
$k = 3$	$\{\mathcal{M}_0, \mathcal{M}_1, \mathcal{M}_2, \mathcal{M}_3\}$	13.35	0.355	0.567	0.260	0.402	0.647

quality and geometric accuracy, suggesting that level 1 provides a more effective latent representation for synthesis. Conversely, using deeper levels (2 or 3) as the boundary leads to a consistent degradation in metrics, likely due to the loss of fine-grained spatial details in abstract feature spaces. Consequently, we fix level 1 as the synthesis boundary k for our full framework, as illustrated in Fig. 2(a). Further analysis of this selection is provided in § 5.5.

4.4 Cascaded Feature Generation

Based on the evaluation in § 4.3, we fix the synthesis boundary at level 1 and generate the corresponding multi-level set. While level 0 can be synthesized independently, generating them separately causes misalignment across the feature hierarchy. To provide the coherent input required by the decoder, we instead employ a cascaded model $\mathcal{M}_{1 \rightarrow 0}$ that synthesizes level 0 conditioned on the generated level 1 latent, which is illustrated in Fig. 2(b). $\mathcal{M}_{1 \rightarrow 0}$ shares the same architecture and training configuration as \mathcal{M}_0 .

To handle the imperfect latents encountered during inference, we train $\mathcal{M}_{1 \rightarrow 0}$ by conditioning on a noisy version of the ground-truth \mathbf{F}_1 . This strategy improves the model’s robustness and ensures $\tilde{\mathbf{F}}_0$ is anchored to $\tilde{\mathbf{F}}_1$, providing the alignment the decoder requires. A quantitative validation of this cascaded approach over independent generation is provided in § 5.6.

5 Experiments

5.1 Setup

Datasets. GLD is trained from scratch on four datasets, RealEstate10K [58] (Re10K), DL3DV [27], HyperSim [35], and TartanAir [50]. Each training sample consists of $V = 8$ views, where 1 to 4 views are randomly selected as source views while the rest are masked as targets. For the main evaluation, we evaluate on two in-domain benchmarks, Re10K and DL3DV, which overlap with the training distribution, and on one out-of-domain object-centric benchmark, Mip-NeRF 360 [3], to evaluate generalization to unseen scene types. We use $N = 2$ source views and measure performance on the target views across 200 samples per dataset. Additional details are provided in Appendix A.3.

Training Details. Our diffusion model operates in the latent space of DA3-Base [26]. We train the diffusion model using AdamW [29] with a fixed learning

Table 3: Quantitative comparison of different methods across in-domain [27, 58] and out-of-domain [3] datasets on 2D and 3D metrics. **Bold** and underlined values indicate the best and second-best results, respectively. We use reproduced CAT3D[†] [22].

Methods	From Scratch	2D Metrics			3D Metrics				
		PSNR \uparrow	SSIM \uparrow	LPIPS \downarrow	ATE \downarrow	RPE _r \downarrow	RPE _t \downarrow	Reproj \downarrow	MEt3R \downarrow
RealEstate10K [58]									
MVGenMaster [4]	X	15.226	0.588	0.456	0.282	6.42	<u>0.526</u>	<u>0.664</u>	0.339
Matrix3D [30]		14.490	0.580	<u>0.448</u>	0.413	8.93	0.638	0.666	0.344
CAMEO [22]		13.800	0.561	0.522	0.446	12.93	0.790	0.661	0.344
NVComposer [24]		11.140	0.418	0.649	0.829	42.85	1.435	0.860	0.457
CAT3D [†] [12]		13.350	0.527	0.561	0.496	17.49	0.941	0.719	0.361
DINO [32]	✓	15.638	0.601	<u>0.448</u>	0.345	15.59	0.719	0.721	0.319
VAE [36]		15.656	0.606	0.456	<u>0.278</u>	8.68	0.552	0.681	0.375
GLD (Ours)		16.362	0.630	0.431	0.211	<u>7.07</u>	0.444	0.673	<u>0.328</u>
DL3DV [27]									
MVGenMaster [4]	X	14.565	0.442	0.460	<u>0.281</u>	<u>6.93</u>	<u>0.592</u>	<u>0.637</u>	0.375
Matrix3D [30]		13.330	0.396	<u>0.451</u>	0.459	9.65	0.850	0.667	0.394
CAMEO [22]		12.320	0.371	0.567	1.143	24.76	2.149	0.706	0.404
NVComposer [24]		10.518	0.273	0.646	1.810	55.59	3.098	0.852	0.517
CAT3D [†] [12]		11.820	0.335	0.594	1.346	31.73	2.473	0.746	0.435
DINO [32]	✓	14.345	0.411	0.471	0.546	13.12	1.050	0.708	0.410
VAE [36]		14.725	<u>0.446</u>	0.476	0.589	15.00	1.116	0.674	0.407
GLD (Ours)		15.499	0.468	0.438	0.209	5.75	0.466	0.612	<u>0.378</u>
Mip-NeRF 360 [3] (Out-of-domain)									
MVGenMaster [4]	X	<u>14.170</u>	0.304	0.511	0.320	10.92	0.587	0.676	<u>0.402</u>
Matrix3D [30]		13.970	0.284	0.483	<u>0.548</u>	<u>13.63</u>	<u>0.948</u>	<u>0.646</u>	0.422
CAMEO [22]		11.900	0.250	0.629	1.623	48.75	3.008	0.684	0.395
NVComposer [24]		12.525	0.217	0.637	1.622	54.26	2.703	0.767	0.526
CAT3D [†] [12]		11.310	0.214	0.653	1.722	54.65	3.171	0.724	0.453
DINO [32]	✓	13.718	0.267	0.542	0.949	27.57	1.720	0.707	0.444
VAE [36]		13.942	0.274	0.548	1.221	35.34	2.200	0.674	0.449
GLD (Ours)		14.542	<u>0.288</u>	<u>0.504</u>	0.589	15.97	1.071	0.630	0.406

rate of 5×10^{-5} , a batch size of 48, and EMA decay of 0.9995. We apply 10% dropout to camera embeddings for classifier-free guidance [15], with a CFG scale of 1.5 at inference. For each sample, the training resolution is randomly chosen from (504×504) , (504×378) , (504×336) , and (504×280) , matching the set of resolutions used to train DA3. GLD is trained on 8 B200 GPUs for 175k iterations. Additional details are provided in Appendix A.1.

Baselines. We compare GLD against two categories of baselines. The first category comprises general-purpose visual encoders, such as VAE [36] and DINO [32], to assess whether the latent space of DA3 [26] is better suited for novel view synthesis than general-purpose visual representations. We additionally evaluate VGGT [47] as an alternative geometric foundation model backbone to further examine the effectiveness of geometry-aware latent spaces for NVS; these results are provided in Appendix C.1. For VAE, we use the Stable Diffusion encoder-decoder [36]. For DINO, we adopt DINOv2 ViT-B/14 with registers [6, 32] as the encoder and train a decoder from scratch. In all cases, the diffusion model is trained from scratch for the same number of iterations using the same architecture as GLD. Additional implementation details are provided in the Appendix A.2.

The second category comprises state-of-the-art diffusion-based NVS methods, including MVGenMaster [4], Matrix3D [30], CAMEO [22], NVComposer [24],

and CAT3D[†] [12]¹. These models typically leverage powerful generative priors by fine-tuning from large-scale pre-trained weights. Note that CAMEO and CAT3D[†] are trained exclusively on the Re10K dataset, whereas the remaining methods incorporate both scene-centric and object-centric data during training.

Evaluation Protocol. We evaluate the 2D image fidelity of generated target views using standard NVS metrics: PSNR, SSIM, and LPIPS. To assess the 3D geometric consistency of generated views, we further incorporate camera estimation errors, reprojection error [9], and MEt3R [2]. Specifically, for camera errors, we extract camera poses from the generated views using an external estimator [47] to compute the Absolute Trajectory Error (ATE), and Relative Pose Errors for rotation (RPE_r) and translation (RPE_t). These camera errors explicitly evaluate condition fidelity by measuring how accurately the generated images adhere to the target pose conditioning. Furthermore, reprojection error and MEt3R quantify the underlying 3D geometric consistency across the generated images. Reprojection error measures the spatial re-alignment accuracy of reconstructed 3D points, while MEt3R evaluates multi-view consistency using projected feature similarity.

5.2 Quantitative Results

2D Metrics. We evaluate image synthesis quality on two in-domain datasets (Re10K and DL3DV) and one zero-shot, out-of-domain benchmark (Mip-NeRF 360). First, we compare our performance against VAE and DINO encoder baselines. As shown in Tab. 3, our method consistently outperforms both baselines in PSNR, SSIM, and LPIPS across all benchmarks. The consistent gains confirm that the DA3 feature space provides a more suitable latent representation for novel view synthesis (NVS) than general-purpose visual encoders.

Second, we evaluate GLD against state-of-the-art NVS methods that leverage massive diffusion priors via large-scale text-to-image (T2I) pretraining. Despite being trained from scratch on smaller datasets, GLD surpasses all baselines across all 2D metrics on both in-domain benchmarks. For the out-of-domain evaluation, which consists mainly of object-centric samples, GLD still achieves state-of-the-art PSNR and highly competitive results across the remaining 2D metrics. This generalization is particularly notable given that GLD is trained exclusively on scene-level data, whereas competing baselines [4, 22, 24] incorporate object-centric datasets [7, 34] during fine-tuning.

3D Metrics. We next evaluate cross-view geometric consistency. As shown in Tab. 3, GLD consistently outperforms the VAE and DINO baselines across most 3D metrics on every benchmark. The most substantial gains are in pose accuracy, where GLD achieves up to a $2.8\times$ lower ATE and a $2.6\times$ lower RPE compared to the baselines. Reprojection error and MEt3R also show consistent improvements across most evaluation settings. These significant improvements

¹ Since the official implementation of CAT3D is unavailable, we use the model and checkpoint reproduced in CAMEO [22].

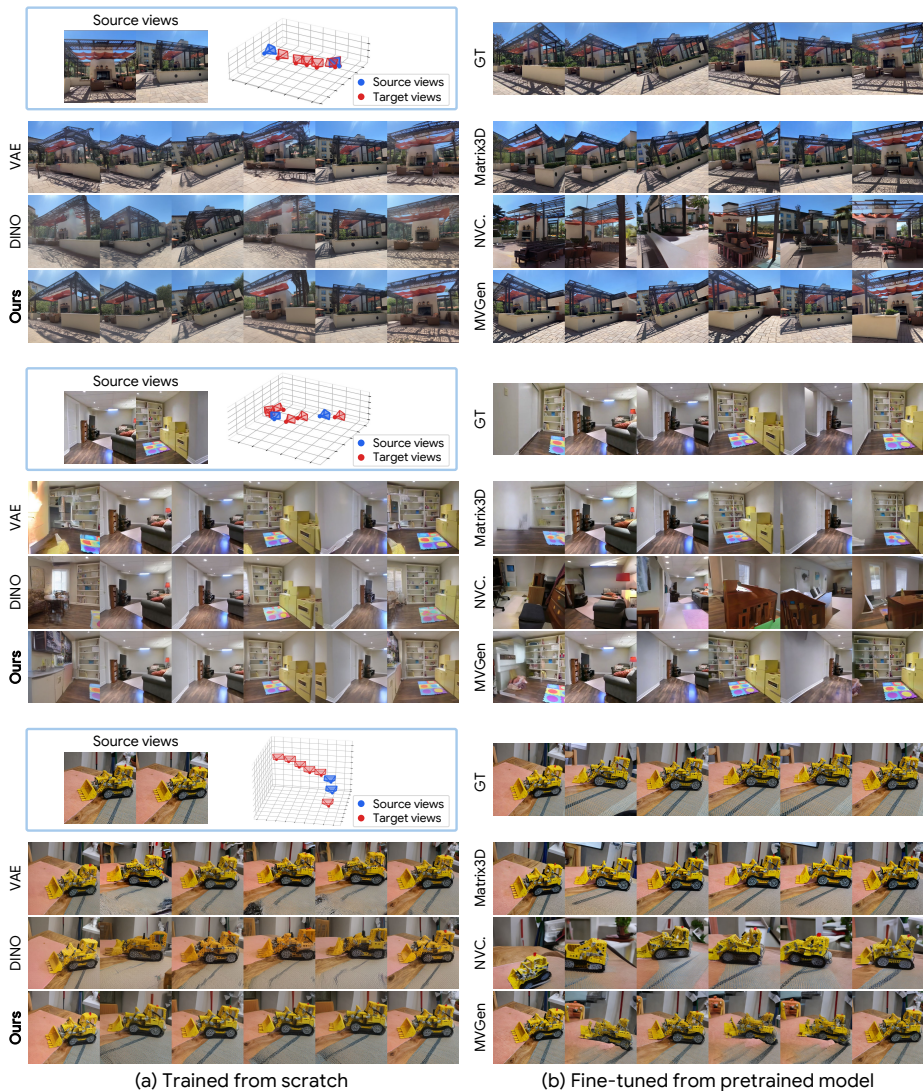


Fig. 4: Qualitative results. We compare the rendering quality of target views given two source views. The rows from top to bottom correspond to the Re10K, DL3DV, and out-of-domain Mip-NeRF 360 datasets, respectively.

compared to VAE and DINO latent spaces demonstrate that GLD yields superior 3D consistency and notably accurate adherence to the target pose.

When compared to most fine-tuned methods, GLD exhibits significantly superior 3D consistency across in-domain benchmarks. This performance gap highlights a fundamental limitation of relying solely on generic T2I priors for NVS. Compared to MVGenMaster, GLD achieves superior performance on DL3DV, while remaining highly competitive on Re10K. Note that MVGenMaster utilizes an external depth estimator [1] and warps source RGB and depth to the

Table 4: Ablation study across different numbers of source images. We report results with $N=1$ and $N=4$ input source views on Re10K and DL3DV. **Bold** values indicate best results.

Source Views	Dataset	Methods	2D Metrics			3D Metrics				
			PSNR \uparrow	SSIM \uparrow	LPIPS \downarrow	ATE \downarrow	RPE _r \downarrow	RPE _t \downarrow	Reproj \downarrow	MEt3R \downarrow
$N=1$	Re10K	DINO [32]	13.49	0.543	0.541	0.442	22.95	0.972	0.735	0.301
		VAE [36]	12.99	0.519	0.566	0.371	12.47	0.718	0.689	0.387
		GLD (Ours)	13.50	0.552	0.541	0.267	8.42	0.539	0.673	0.306
	DL3DV	DINO [32]	12.80	0.368	0.539	0.743	20.14	1.405	0.738	0.418
		VAE [36]	12.47	0.360	0.569	0.880	25.93	1.828	0.702	0.420
		GLD (Ours)	13.03	0.385	0.543	0.237	6.14	0.512	0.619	0.375
$N=4$	Re10K	DINO [32]	17.73	0.651	0.365	0.221	7.92	0.482	0.685	0.327
		VAE [36]	18.68	0.695	0.348	0.200	6.26	0.407	0.655	0.347
		GLD (Ours)	19.00	0.696	0.327	0.182	6.69	0.397	0.653	0.327
	DL3DV	DINO [32]	15.44	0.443	0.423	0.274	7.49	0.563	0.667	0.408
		VAE [36]	16.37	0.505	0.410	0.294	8.14	0.556	0.643	0.406
		GLD (Ours)	17.09	0.517	0.378	0.143	3.74	0.305	0.601	0.385

target view as condition inputs, making it heavily reliant on explicit, dense geometric priors. In contrast, GLD operates in a multi-view geometry-aware latent space without requiring explicit geometry conditions (*e.g.*, depth maps) during inference. Although GLD achieves slightly lower pose accuracy on the out-of-domain benchmark than Matrix3D and MVGenMaster, this is expected, as those baselines benefit from strong T2I priors and are additionally fine-tuned on object-centric datasets. Despite relying exclusively on scene-level training without external warping, GLD still achieves the lowest reprojection error and a competitive MEt3R score. This shows that our DA3 latent space effectively encodes the geometric structures necessary for robust, coherent multi-view NVS.

5.3 Qualitative Results

Fig. 4 presents qualitative comparisons of generated target views. The left column (a) shows methods trained from scratch, while the right column (b) shows methods fine-tuned from pretrained T2I models. GLD produces structurally coherent views that closely follow the ground-truth layout, outperforming the VAE and DINOv2 baselines particularly under large viewpoint changes, and remaining competitive with fine-tuned methods despite not leveraging T2I pretraining. We note that the method that relies on warped source views from an external geometry estimator [4] produces sharp outputs but can exhibit noticeable artifacts when the estimation fails, as seen in the fourth column of the first scene, whereas GLD avoids such failure modes. Additional qualitative results are provided in Appendix C.3.

5.4 Decoder Performance

We train the ViT-based RGB decoder, \mathcal{D}_{rgb} , on a combined dataset of Re10K [58] and DL3DV [27]. Following RAE [56], the model is optimized using a weighted sum of \mathcal{L}_1 , LPIPS, and adversarial losses. We utilize the AdamW optimizer and a cosine learning rate scheduler with a 1-epoch warmup.

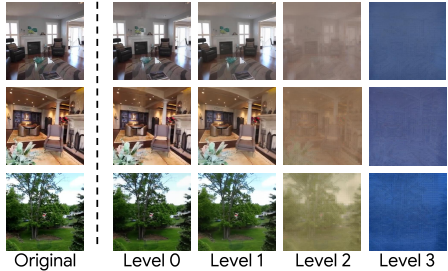
The decoder is trained using a multi-resolution strategy involving resolutions of (504, 504), (504, 378), (504, 336), and (504, 280). We employ a global batch size

Table 5: Geometric Correspondence. PCK results for each DA3 level and DINOv2 [32].

Feature	F_0	F_1	F_2	F_3	DINOv2
PCK \uparrow	22.25	<u>35.98</u>	40.70	20.98	31.64

Table 6: Reconstruction Fidelity. Reconstruction comparison via PSNR and LPIPS across different DA3 [26] levels.

Feature	F_0	F_1	F_2	F_3
PSNR \uparrow	28.01	<u>25.36</u>	14.01	10.19
SSIM \uparrow	0.922	<u>0.873</u>	0.627	0.508
LPIPS \downarrow	0.138	<u>0.138</u>	<u>0.491</u>	0.768

**Fig. 5: Reconstruction Visualization.** Qualitative comparison showing the reconstruction results for different levels.

of 128 and an EMA decay of 0.9978. The entire training process is conducted on 8 NVIDIA B200 GPUs, spanning approximately 170k steps. For further comparison, we additionally train a baseline RAE decoder on DINOv2 [32] features using the same architecture and training configuration.

In Tab. 7, we compare \mathcal{D}_{rgb} with the standard pretrained VAEs used in Stable Diffusion [36] and SDXL [33]. Our decoder reconstructs high-fidelity images from DA3 features and performs competitively with these widely used models. These results indicate that multi-level DA3 features form a sufficiently expressive latent space for high-quality image synthesis.

5.5 Discussion on Boundary Layer Selection

In § 4.3, we found that boundary layer $k = 1$ yields the best NVS performance. To understand why, we analyze the four levels of features (levels 0 to 3). Specifically, we examine features from geometric and photometric perspectives by measuring their cross-view correspondence and their capacity for high-fidelity image reconstruction, respectively.

For geometric correspondence, we follow the evaluation protocol in Probe3D [10] and assess features on the ScanNet [5] dataset using PCK, the fraction of points that are correctly matched within a distance threshold. Our results in Tab. 5 show that level 1 and level 2 achieve high PCK scores, even outperforming DINOv2 [32]. This indicates that these levels encode stable 3D structures. In contrast, level 0 exhibits poor correspondence; being the shallowest layer, it does not encode the complex geometric relationships needed for cross-view matching.

To evaluate photometric information, we utilize the RGB decoder \mathcal{D}_{rgb} from § 4.2 to reconstruct the original image. Because \mathcal{D}_{rgb} is trained with layer dropout, it is capable of reconstructing images from a single feature level. By reconstructing from each level independently and measuring the error, we find that levels 0 and 1 retain rich appearance cues, producing accurate colors and textures. However, deeper features, such as level 2, discard essential photometric

Table 7: Reconstruction Fidelity Comparison. We evaluate the reconstruction quality using 4,000 randomly sampled images from the Re10K [58] test set.

Methods	PSNR \uparrow	SSIM \uparrow	LPIPS \downarrow
VAE [36]	34.53	0.939	0.028
VAE (SDXL) [33]	34.97	0.945	0.029
RAE (DINO) [56]	26.78	0.830	0.148
DA3 Dec. (\mathcal{D}_{rgb})	35.41	0.960	0.019

Table 8: Cascaded vs. Independent Generation. We evaluate NVS performance on Re10K with $N=4$ source views.

Methods	2D Metrics			3D Metrics				
	PSNR \uparrow	SSIM \uparrow	LPIPS \downarrow	ATE \downarrow	RPE _r \downarrow	RPE _t \downarrow	Reproj \downarrow	MEt3R \downarrow
Independent	18.81	0.692	0.335	0.197	7.179	0.430	0.666	0.335
Cascaded (Ours)	19.00	0.695	0.327	0.182	6.694	0.397	0.652	0.326

details. This results in noticeable color loss and smoothed textures (Fig. 5), as well as a notable drop in PSNR compared to shallower levels (Tab. 6).

These results indicate that level 1 successfully meets both requirements. It maintains a high degree of geometric alignment comparable to level 2, while retaining substantially more photometric information than the deeper features. This observation provides a straightforward explanation for why level 1 serves as the optimal latent space for our NVS framework.

5.6 Ablation Studies

Varying the Number of Source Images. In this section, we evaluate the robustness of GLD under varying numbers of source views by comparing against the VAE [36] and DINOv2 [32] baselines. Following the evaluation protocol from our main experiments, we present the quantitative results in Tab. 4. Notably, the margin of improvement in 3D metrics grows as the number of source views decreases. For instance, on DL3DV with $N=1$, GLD achieves over $3\times$ lower ATE and RPE_r compared to both baselines, whereas with $N=4$ the gap is approximately $2\times$. This trend is consistent across both datasets, suggesting that the geometric priors in the DA3 feature space become particularly beneficial when fewer visual cues are available.

Effectiveness of the Cascaded Design. In § 4.4, we generate $\tilde{\mathbf{F}}_0$ by conditioning on the previously synthesized $\tilde{\mathbf{F}}_1$ to ensure consistency across feature levels. To validate this design, we compare against an independent baseline where \mathcal{M}_0 and \mathcal{M}_1 generate their respective features without seeing each other’s output. As shown in Tab. 8, evaluated on Re10K with $N=4$ source views, the cascading approach consistently improves both 2D and 3D metrics, confirming that allowing shallower features to be conditioned by deeper ones leads to more coherent multi-level representations.

5.7 Geometry Evaluation

Since GLD generates the multi-level DA3 features, we can leverage the original, pretrained DPT-based decoder \mathcal{D}_{DA3} to predict ray and depth maps without any additional training or fine-tuning. This allows us to obtain dense geometric predictions as a zero-shot byproduct of the generation process. We evaluate the fidelity of these maps through depth metrics and 3D point-cloud visualizations.

Table 9: Depth Evaluation. Comparison with Matrix3D [30] on ETH3D [39].

Methods	Depth			RGB
	AbsRel \downarrow	SqRel \downarrow	$\delta_1\uparrow$	PSNR \uparrow
Matrix3D [30]	0.197	0.475	0.731	14.13
GLD (Ours)	0.160	0.410	0.800	14.80

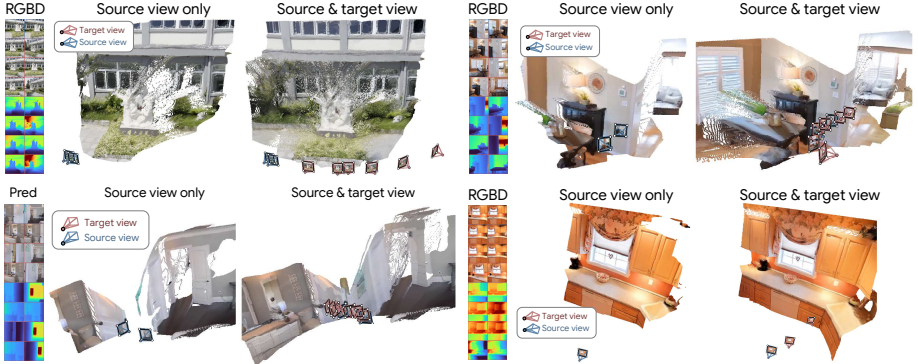


Fig. 6: 3D Reconstruction Visualization. We unproject the synthesized novel views into 3D space using the jointly generated depth and ray maps.

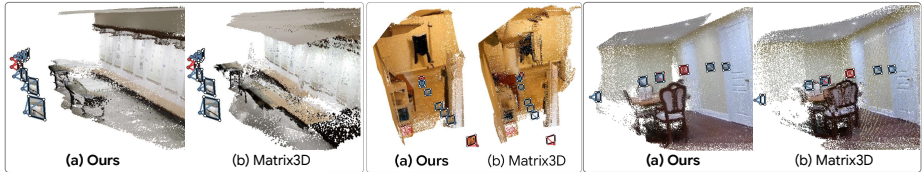


Fig. 7: 3D Reconstruction Comparison: Point clouds unprojected from source and target views RGBD outputs of GLD and Matrix3D [30].

Depth Evaluation. We compare our generated depth maps against Matrix3D [30], which jointly generates depth and RGB images. We evaluate performance on the ETH3D dataset [39], which provides high-quality ground-truth depth maps. As shown in Tab. 9, our model produces more accurate depth estimates, suggesting that operating in the DA3 latent space provides effective geometry grounding.

3D Reconstruction Visualization. We visualize the 3D reconstruction by unprojecting the synthesized pixels into 3D space using the generated depth and ray maps. As illustrated in Fig. 6, the resulting point clouds exhibit consistent 3D geometry across diverse camera trajectories, confirming that our generated latent features are geometrically coherent with the underlying scene. We further compare against Matrix3D [30] in Fig. 7. While Matrix3D produces noticeable geometric distortions, GLD yields significantly cleaner and more coherent reconstructions, consistent with the quantitative results in Tab. 9.

6 Conclusion

We presented **Geometric Latent Diffusion (GLD)**, a framework that repurposes the feature space of a geometric foundation model as the latent space for novel view synthesis. Through systematic analysis, we identified a feature level that balances geometric correspondence and photometric fidelity and showed that training diffusion models in this space yields consistent improvements in

both 2D image quality and 3D consistency over standard VAE and DINOv2 latent spaces. GLD achieves competitive performance with state-of-the-art methods that leverage large-scale text-to-image pretraining, despite being trained entirely from scratch, while also enabling zero-shot depth and 3D reconstruction as a natural byproduct of the generation process. We hope that this work encourages further investigation into task-specific latent space design for geometry-aware generation.

Acknowledgment

This work was completed during WJ and JH’s visit to NYU as part of the Global AI Frontier Lab Program. S.X. acknowledges support from Intel Labs, the MSIT IITP grant (RS-2024-00457882) and the NSF award IIS-2443404.

References

1. Depth pro: Sharp monocular metric depth in less than a second. In: ICLR (2025), <https://arxiv.org/abs/2410.02073>
2. Asim, M., Wewer, C., Wimmer, T., Schiele, B., Lenssen, J.E.: Met3r: Measuring multi-view consistency in generated images. In: CVPR (2025)
3. Barron, J.T., Mildenhall, B., Verbin, D., Srinivasan, P.P., Hedman, P.: Mip-nerf 360: Unbounded anti-aliased neural radiance fields. In: CVPR. pp. 5470–5479 (2022)
4. Cao, C., Yu, C., Liu, S., Wang, F., Xue, X., Fu, Y.: Mygenmaster: Scaling multi-view generation from any image via 3d priors enhanced diffusion model. In: CVPR. pp. 6045–6056 (2025)
5. Dai, A., Chang, A.X., Savva, M., Halber, M., Funkhouser, T., Nießner, M.: Scannet: Richly-annotated 3d reconstructions of indoor scenes. In: CVPR. pp. 5828–5839 (2017)
6. Darcet, T., Oquab, M., Mairal, J., Bojanowski, P.: Vision transformers need registers. arXiv preprint arXiv:2309.16588 (2023)
7. Deitke, M., Schwenk, D., Salvador, J., Weihs, L., Michel, O., VanderBilt, E., Schmidt, L., Ehsani, K., Kembhavi, A., Farhadi, A.: Objaverse: A universe of annotated 3d objects. In: CVPR. pp. 13142–13153 (2023)
8. Dosovitskiy, A., Beyer, L., Kolesnikov, A., Weissenborn, D., Zhai, X., Unterthiner, T., Dehghani, M., Minderer, M., Heigold, G., Gelly, S., et al.: An image is worth 16x16 words: Transformers for image recognition at scale. arXiv preprint arXiv:2010.11929 (2020)
9. Du, H., Ye, J., Cong, X., Li, R., Ni, J., Agarwal, A., Zhou, Z., Li, Z., Balestrieri, R., Wang, Y.: Videogpa: Distilling geometry priors for 3d-consistent video generation. arXiv preprint arXiv:2601.23286 (2026)
10. El Banani, M., Raj, A., Maninis, K.K., Kar, A., Li, Y., Rubinstein, M., Sun, D., Guibas, L., Johnson, J., Jampani, V.: Probing the 3d awareness of visual foundation models. In: CVPR. pp. 21795–21806 (2024)
11. Esser, P., Rombach, R., Ommer, B.: Taming transformers for high-resolution image synthesis. In: CVPR. pp. 12873–12883 (2021)
12. Gao, R., Holynski, A., Henzler, P., Brussee, A., Martin-Brualla, R., Srinivasan, P., Barron, J.T., Poole, B.: Cat3d: Create anything in 3d with multi-view diffusion models. arXiv preprint arXiv:2405.10314 (2024)
13. Han, J., Hong, S., Jung, J., Jang, W., An, H., Wang, Q., Kim, S., Feng, C.: Emergent outlier view rejection in visual geometry grounded transformers. arXiv preprint arXiv:2512.04012 (2025)
14. Ho, J., Jain, A., Abbeel, P.: Denoising diffusion probabilistic models. *NeurIPS* **33**, 6840–6851 (2020)
15. Ho, J., Salimans, T.: Classifier-free diffusion guidance. arXiv preprint arXiv:2207.12598 (2022)
16. Keetha, N., Müller, N., Schönberger, J., Porzi, L., Zhang, Y., Fischer, T., Knapitsch, A., Zauss, D., Weber, E., Antunes, N., et al.: Mapanything: Universal feed-forward metric 3d reconstruction. arXiv preprint arXiv:2509.13414 (2025)
17. Kerbl, B., Kopanas, G., Leimkühler, T., Drettakis, G., et al.: 3d gaussian splatting for real-time radiance field rendering. *ACM TOG* **42**(4), 139–1 (2023)
18. Kingma, D.P., Welling, M.: Auto-encoding variational bayes. arXiv preprint arXiv:1312.6114 (2013)

19. Kong, X., Watson, D., Strümler, Y., Niemeyer, M., Tombari, F.: Causnvs: Autoregressive multi-view diffusion for flexible 3d novel view synthesis. arXiv preprint arXiv:2509.06579 (2025)
20. Krishnan, A., Yan, X., Casser, V., Kundu, A.: Orchid: Image latent diffusion for joint appearance and geometry generation. In: ICCV. pp. 28217–28227 (2025)
21. Kwak, M.S., Kim, J., Yun, S., Han, D., Kim, T., Kim, S., Kim, J.H.: Aligned novel view image and geometry synthesis via cross-modal attention instillation. arXiv preprint arXiv:2506.11924 (2025)
22. Kwon, M., Choi, J., Park, J., Jeon, S., Jang, J., Seo, J., Kwak, M., Kim, J.H., Kim, S.: Cameo: Correspondence-attention alignment for multi-view diffusion models. arXiv preprint arXiv:2512.03045 (2025)
23. Labs, B.F.: Flux. <https://github.com/black-forest-labs/flux> (2024)
24. Li, L., Zhang, Z., Li, Y., Xu, J., Hu, W., Li, X., Cheng, W., Gu, J., Xue, T., Shan, Y.: Nvcomposer: Boosting generative novel view synthesis with multiple sparse and unposed images. In: CVPR. pp. 777–787 (2025)
25. Li, R., Yi, B., Liu, J., Gao, H., Ma, Y., Kanazawa, A.: Cameras as relative positional encoding. In: NeurIPS (2025)
26. Lin, H., Chen, S., Liew, J., Chen, D.Y., Li, Z., Shi, G., Feng, J., Kang, B.: Depth anything 3: Recovering the visual space from any views. arXiv preprint arXiv:2511.10647 (2025)
27. Ling, L., Sheng, Y., Tu, Z., Zhao, W., Xin, C., Wan, K., Yu, L., Guo, Q., Yu, Z., Lu, Y., et al.: D13dv-10k: A large-scale scene dataset for deep learning-based 3d vision. In: CVPR. pp. 22160–22169 (2024)
28. Lipman, Y., Chen, R.T.Q., Ben-Hamu, H., Nickel, M., Le, M.: Flow matching for generative modeling. In: ICLR (2023)
29. Loshchilov, I., Hutter, F.: Decoupled weight decay regularization. arXiv preprint arXiv:1711.05101 (2017)
30. Lu, Y., Zhang, J., Fang, T., Nahmias, J.D., Tsin, Y., Quan, L., Cao, X., Yao, Y., Li, S.: Matrix3d: Large photogrammetry model all-in-one. CVPR (2025)
31. Mildenhall, B., Srinivasan, P.P., Tancik, M., Barron, J.T., Ramamoorthi, R., Ng, R.: Nerf: Representing scenes as neural radiance fields for view synthesis. *Communications of the ACM* **65**(1), 99–106 (2021)
32. Oquab, M., Darcet, T., Moutakanni, T., Vo, H., Szafraniec, M., Khalidov, V., Fernandez, P., Haziza, D., Massa, F., El-Nouby, A., et al.: Dinov2: Learning robust visual features without supervision. arXiv preprint arXiv:2304.07193 (2023)
33. Podell, D., English, Z., Lacey, K., Blattmann, A., Dockhorn, T., Müller, J., Penna, J., Rombach, R.: Sdxl: Improving latent diffusion models for high-resolution image synthesis. arXiv preprint arXiv:2307.01952 (2023)
34. Reizenstein, J., Shapovalov, R., Henzler, P., Sbordone, L., Labatut, P., Novotny, D.: Common objects in 3d: Large-scale learning and evaluation of real-life 3d category reconstruction. In: ICCV. pp. 10901–10911 (2021)
35. Roberts, M., Ramapuram, J., Ranjan, A., Kumar, A., Bautista, M.A., Paczan, N., Webb, R., Susskind, J.M.: Hypersim: A photorealistic synthetic dataset for holistic indoor scene understanding. In: ICCV (2021)
36. Rombach, R., Blattmann, A., Lorenz, D., Esser, P., Ommer, B.: High-resolution image synthesis with latent diffusion models. In: CVPR. pp. 10684–10695 (2022)
37. Sauer, A., Karras, T., Laine, S., Geiger, A., Aila, T.: Stylegan-t: Unlocking the power of gans for fast large-scale text-to-image synthesis. In: ICML. pp. 30105–30118. PMLR (2023)
38. Schonberger, J.L., Frahm, J.M.: Structure-from-motion revisited. In: CVPR. pp. 4104–4113 (2016)

39. Schöps, T., Schönberger, J.L., Galliani, S., Sattler, T., Schindler, K., Pollefeys, M., Geiger, A.: A multi-view stereo benchmark with high-resolution images and multi-camera videos. In: CVPR (2017)
40. Seo, J., Fukuda, K., Shibuya, T., Narihira, T., Murata, N., Hu, S., Lai, C.H., Kim, S., Mitsufuji, Y.: Genwarp: Single image to novel views with semantic-preserving generative warping. *NeurIPS* **37**, 80220–80243 (2024)
41. Shi, M., Wang, H., Zheng, W., Yuan, Z., Wu, X., Wang, X., Wan, P., Zhou, J., Lu, J.: Latent diffusion model without variational autoencoder. *arXiv preprint arXiv:2510.15301* (2025)
42. Shi, Y., Wang, P., Ye, J., Long, M., Li, K., Yang, X.: Mvdream: Multi-view diffusion for 3d generation. *arXiv preprint arXiv:2308.16512* (2023)
43. Siméoni, O., Vo, H.V., Seitzer, M., Baldassarre, F., Oquab, M., Jose, C., Khalidov, V., Szafraniec, M., Yi, S., Ramamonjisoa, M., Massa, F., Haziza, D., Wehrstedt, L., Wang, J., Darcet, T., Moutakanni, T., Sentana, L., Roberts, C., Vedaldi, A., Tolan, J., Brandt, J., Couprie, C., Mairal, J., Jégou, H., Labatut, P., Bojanowski, P.: Dinov3 (2025), <https://arxiv.org/abs/2508.10104>
44. Song, Y., Sohl-Dickstein, J., Kingma, D.P., Kumar, A., Ermon, S., Poole, B.: Score-based generative modeling through stochastic differential equations. *arXiv preprint arXiv:2011.13456* (2020)
45. Tong, S., Zheng, B., Wang, Z., Tang, B., Ma, N., Brown, E., Yang, J., Fergus, R., LeCun, Y., Xie, S.: Scaling text-to-image diffusion transformers with representation autoencoders. *arXiv preprint arXiv:2601.16208* (2026)
46. Tschannen, M., Gritsenko, A., Wang, X., Naeem, M.F., Alabdulmohsin, I., Parthasarathy, N., Evans, T., Beyer, L., Xia, Y., Mustafa, B., et al.: Siglip 2: Multilingual vision-language encoders with improved semantic understanding, localization, and dense features. *arXiv preprint arXiv:2502.14786* (2025)
47. Wang, J., Chen, M., Karaev, N., Vedaldi, A., Rupprecht, C., Novotny, D.: Vggg: Visual geometry grounded transformer. In: CVPR. pp. 5294–5306 (2025)
48. Wang, S., Tian, Z., Huang, W., Wang, L.: Ddt: Decoupled diffusion transformer. *arXiv preprint arXiv:2504.05741* (2025)
49. Wang, S., Leroy, V., Cabon, Y., Chidlovskii, B., Revaud, J.: Dust3r: Geometric 3d vision made easy. In: CVPR. pp. 20697–20709 (2024)
50. Wang, W., Zhu, D., Wang, X., Hu, Y., Qiu, Y., Wang, C., Hu, Y., Kapoor, A., Scherer, S.: Tartanair: A dataset to push the limits of visual slam (2020)
51. Wang, Y., Zhou, J., Zhu, H., Chang, W., Zhou, Y., Li, Z., Chen, J., Pang, J., Shen, C., He, T.: π^3 : Permutation-equivariant visual geometry learning. *arXiv preprint arXiv:2507.13347* (2025)
52. Yang, Y., Shao, J., Li, X., Shen, Y., Geiger, A., Liao, Y.: Prometheus: 3d-aware latent diffusion models for feed-forward text-to-3d scene generation. In: CVPR. pp. 2857–2869 (2025)
53. Yu, W., Xing, J., Yuan, L., Hu, W., Li, X., Huang, Z., Gao, X., Wong, T.T., Shan, Y., Tian, Y.: Viewcrafter: Taming video diffusion models for high-fidelity novel view synthesis. *arXiv preprint arXiv:2409.02048* (2024)
54. Zhang, R., Isola, P., Efros, A.A., Shechtman, E., Wang, O.: The unreasonable effectiveness of deep features as a perceptual metric. In: CVPR. pp. 586–595 (2018)
55. Zhao, S., Liu, Z., Lin, J., Zhu, J.Y., Han, S.: Differentiable augmentation for data-efficient gan training. *NeurIPS* **33**, 7559–7570 (2020)
56. Zheng, B., Ma, N., Tong, S., Xie, S.: Diffusion transformers with representation autoencoders. *arXiv preprint arXiv:2510.11690* (2025)

57. Zhou, J., Gao, H., Voleti, V., Vasishtha, A., Yao, C.H., Boss, M., Torr, P., Rupprecht, C., Jampani, V.: Stable virtual camera: Generative view synthesis with diffusion models. In: ICCV. pp. 12405–12414 (2025)
58. Zhou, T., Tucker, R., Flynn, J., Fyffe, G., Snavely, N.: Stereo magnification: Learning view synthesis using multiplane images. *ACM TOG* **37** (2018), <https://arxiv.org/abs/1805.09817>

Appendix

A Implementation Details

A.1 Training Details

This subsection describes the training configurations. Hyperparameters are summarized in Tab. 11.

RGB Decoder. We train the RGB decoder \mathcal{D}_{rgb} on images of varying resolutions, including (504×504) , (504×378) , (504×336) , and (504×280) . Following RAE [56], we optimize the decoder using ℓ_1 , LPIPS [54], and GAN losses [37]. The reconstruction losses are weighted equally, while the GAN loss is scaled with an adaptive weight [11] to balance reconstruction and adversarial supervision. For the discriminator, we adopt the same setup as StyleGAN-T [37] and apply differentiable augmentations [55] before feeding images to the discriminator.

Multi-view Diffusion. For classifier-free guidance (CFG) [15], camera embeddings are dropped by zeroing the Plücker ray embeddings and setting the extrinsic matrices to identity in PRoPE [25]. To handle varying image resolutions, input resolutions are sampled per batch from (504×504) , (504×378) , (504×336) , and (504×280) with ratio $2 : 2 : 1 : 1$. Each training batch consists of 48 scenes, each containing $V = 8$ views.

Some vision encoders produce additional non-spatial tokens, such as register tokens in DINOv2 [6, 32] and camera tokens in VGGT [47] and DA3 [26]. While our architecture can jointly denoise these tokens via dedicated embedders, we omitted them from our final experiments for simplicity, as the downstream decoders operate exclusively on spatial features.

A.2 Architecture Details

This subsection details the implementation of each module introduced in §4. The full architecture is illustrated in Fig. 8.

RGB Decoder. We utilize a ViT-based RGB decoder with a patch size of 14. The model is built with 12 transformer layers, an intermediate dimension of 3072, and a dropout probability of 0.5. The decoder learns to reconstruct RGB images from the geometric latent features. The architecture is illustrated in Fig. 8(B).

Multi-Level Feature Extraction. Given V input views, the frozen geometric encoder $\mathcal{E}_{\text{geo}}(\cdot)$ extracts $L=4$ feature levels, where T is the token sequence length at the encoder patch resolution and $C=1536$ is the channel dimension. The four levels correspond to intermediate outputs of the frozen DA3-Base backbone

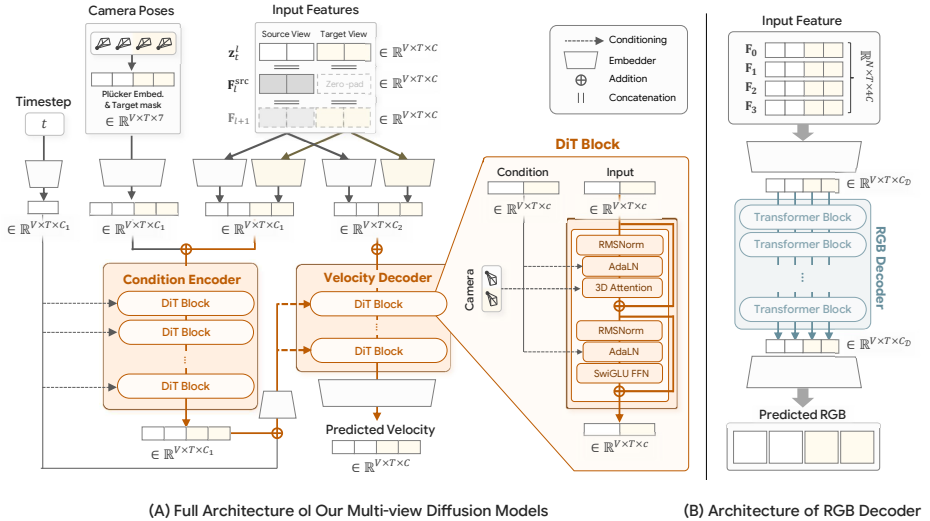


Fig. 8: Architecture details. (A) Our multi-view diffusion model, featuring a condition encoder and a velocity decoder conditioned on camera poses and multi-view features. (B) The RGB decoder architecture that maps the multi-level latent features back to the pixel space.

after blocks $\{5, 7, 9, 11\}$, matching the multi-scale outputs consumed by the DA3 decoder. Before diffusion training, each level is normalized to zero mean and unit variance using channel-wise statistics precomputed on the training set. The inverse transform is applied before decoding.

Multi-view Diffusion Model. As illustrated in Fig. 8(A), each level-wise diffusion model follows the DiT^{DH} [48] architecture, which decouples the network into two components: a **condition encoder** and a **velocity decoder**.

The condition encoder processes the input tokens with a hidden dimension $C_1=768$ through 28 DiT blocks, producing a compact representation that summarizes the source–target context. The velocity decoder uses a larger hidden dimension $C_2=2048$ and predicts the velocity field $\mathbf{u}_{t,l} \in \mathbb{R}^{V \times T \times C}$. For the level-wise models \mathcal{M}_l , the velocity decoder consists of 6 DiT blocks, whereas for the cascaded model $\mathcal{M}_{1 \rightarrow 0}$, it consists of 2 DiT blocks. The encoder’s output conditions the decoder via AdaLN modulation, and camera information is injected into the decoder through addition. All models share the same overall design, while the cascaded model $\mathcal{M}_{1 \rightarrow 0}$ uses a shallower velocity decoder.

The model receives the noisy latent \mathbf{z}_t^l concatenated channel-wise with the source-only condition $\mathbf{F}_l^{\text{src}}$ (zero-padded for target views). For the cascaded model $\mathcal{M}_{1 \rightarrow 0}$, the condition encoder receives the source-only condition and the deeper level features \mathbf{F}_{l+1} . Since source views have clean features while target views are zero-padded, we use separate patch embedders for each view type in both the encoder and decoder, yielding four embedders in total. These embed-

Table 10: DiT^{DH} configuration used for all level-wise diffusion models in GLD.

Parameter	Condition Encoder	Velocity Decoder
Hidden dimension	$C_1 = 768$	$C_2 = 2048$
Number of blocks	28	6 (\mathcal{M}_l), 2 ($\mathcal{M}_{1 \rightarrow 0}$)
Attention heads	16	16
MLP activation	SwiGLU	SwiGLU
Normalization	RMSNorm	RMSNorm
Input channels	$2C = 3072$ (\mathcal{M}_l)	
Output channels	$C = 1536$	
Patch size	1 (DA3, DINO), 2 (VAE)	
Positional encoding	PRoPE [25]	

ders tokenize the latent feature maps and project them from $2C$ channels to C_1 or C_2 : for DA3 latents, we use a patch size of 1 to preserve the original token resolution, whereas for VAE latents, we use a patch size of 2 to reduce the token count due to their higher spatial resolution.

After embedding, all view tokens are concatenated along the view dimension and processed jointly through DiT blocks [48], in which standard self-attention is replaced with 3D self-attention to enable cross-view interactions.

For camera conditioning, we compute per-pixel 6D Plücker coordinates from the camera intrinsics and extrinsics, concatenate a binary source/target indicator $\mathbf{m} \in \{0, 1\}^{V \times T \times 1}$ (0 for source views and 1 for target views) to form a 7D embedding, and project it to the hidden dimension via a linear layer. PRoPE [25] is applied in every 3D self-attention layer.

Table 11: Training configuration for decoder and discriminator.

Component	Decoder \mathcal{D}_{rgb}	Multi-view Diffusion
optimizer	Adam	AdamW
max learning rate	2×10^{-4}	5×10^{-5}
min learning rate	2×10^{-5}	5×10^{-5}
learning rate schedule	cosine decay	constant
optimizer betas	(0.9, 0.95)	(0.9, 0.95)
weight decay	0.0	0.0
batch size	16	48
warmup	1 epoch	–
loss	$\ell_1 + \text{LPIPS} + \text{GAN}$	v-prediction
Model	ViT-XL	DiT ^{DH}
EMA decay	0.9978	0.9995
gradient clipping	–	1.0

Table 12: Number of scenes per dataset used for training and evaluation.

Dataset	Train	Eval
Re10K [58]	66,033	200
DL3DV [27]	10,176	55
HyperSim [35]	794	–
TartanAir [50]	369	–
MipNeRF-360 [3]	–	9
ETH3D [39]	–	13

A.3 Dataset Details

RGB Decoder. We train the RGB decoder on Re10K [58] and DL3DV [27], sampling the two datasets at an equal ratio. For evaluation, we randomly sample 500 scenes, each with 8 views, resulting in 4,000 images in total. All images are resized to a resolution of 504×504 .

Multi-view Diffusion Model. We train GLD on four datasets: Re10K [58], DL3DV [27], HyperSim [35], and TartanAir [50], with a mixing ratio of 4 : 4 : 1 : 1. We use Mip-NeRF 360 [3] for out-of-domain evaluation and ETH3D [39] for depth evaluation. To handle varying scene scales across datasets, all camera poses are normalized relative to the last view, which is set as the origin, and scaled such that the maximum camera distance within the batch is 1. The multi-view sequence starts from a randomly sampled frame index chosen to ensure sufficient remaining frames for the required number of views, with each consecutive frame interval independently and uniformly sampled within a predefined range. For interpolation, the first and last frames are always included as source views when $N = 2$, while additional source views are placed at uniform intervals when $N > 2$.

For evaluation, we use 200 samples per dataset from Re10K, DL3DV, and Mip-NeRF 360 for NVS, and 50 samples from ETH3D for depth evaluation. For datasets whose evaluation sets contain fewer scenes than the target count [3, 27, 39], multiple samples are drawn from the same scene using randomized view sampling. Dataset statistics are summarized in Tab. 12.

B Evaluation Details

B.1 Baseline Adaptation

In this section, we describe how each baseline is adapted for our evaluation. For all baselines, we use the default CFG scale provided in the official repositories. We also resize the generated images from 512×512 to 504×504 to match GLD’s output resolution and ensure a fair comparison.

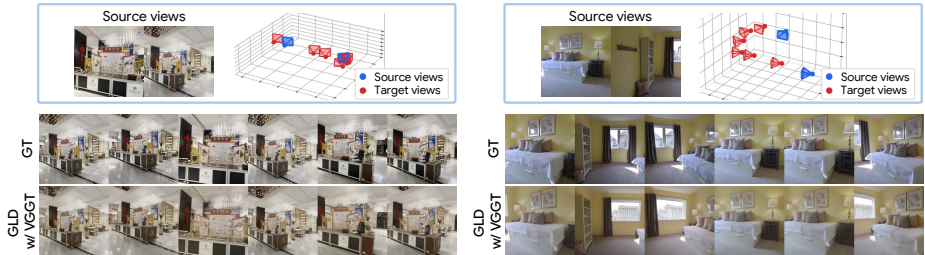


Fig. 9: Qualitative results of GLD w/ VGGT.

Table 13: Quantitative comparison of GLD using DA3 [26] and VGGT [47] backbones against baseline latent representations across in-domain [27, 58] and out-of-domain [3] datasets on 2D and 3D metrics. **Bold** and underlined values indicate the best and second-best results, respectively.

Methods	2D Metrics			3D Metrics				
	PSNR \uparrow	SSIM \uparrow	LPIPS \downarrow	ATE \downarrow	RPE _r \downarrow	RPE _t \downarrow	Reproj \downarrow	MEt3R \downarrow
RealEstate10K [58]								
DINO [32]	15.64	0.601	0.448	0.345	15.59	0.719	0.721	0.319
VAE [36]	15.66	<u>0.606</u>	0.456	0.278	8.68	0.552	0.681	0.375
GLD w/ VGGT [47]	<u>16.17</u>	0.596	0.429	<u>0.216</u>	<u>7.17</u>	0.440	0.666	<u>0.325</u>
GLD w/ DA3 [26]	16.36	0.630	<u>0.431</u>	0.211	7.07	<u>0.444</u>	<u>0.673</u>	0.328
DL3DV [27]								
DINO [32]	14.35	0.411	0.471	0.546	13.12	1.050	0.708	0.410
VAE [36]	14.73	<u>0.446</u>	0.476	0.589	15.00	1.116	0.674	0.407
GLD w/ VGGT [47]	<u>15.25</u>	0.434	0.436	0.188	5.23	0.462	<u>0.634</u>	<u>0.386</u>
GLD w/ DA3 [26]	15.50	0.468	0.438	<u>0.209</u>	<u>5.75</u>	<u>0.466</u>	0.612	0.378
Mip-NeRF 360 [3] (Out-of-domain)								
DINO [32]	13.72	0.267	0.542	0.949	27.57	1.720	0.707	0.444
VAE [36]	<u>13.94</u>	<u>0.274</u>	0.548	1.221	35.34	2.200	0.674	0.449
GLD w/ VGGT [47]	13.57	0.265	0.529	<u>0.596</u>	<u>16.58</u>	<u>1.190</u>	<u>0.654</u>	0.394
GLD w/ DA3 [26]	14.54	0.288	0.504	0.589	15.97	1.071	0.630	<u>0.405</u>

MVGenMaster. MVGenMaster [4] requires metric depth for the reference views, warped RGB, and warped depth for the target view as input conditioning. Since metric depth is not provided in their evaluation setting, we leverage Depth Anything 3 [26] to estimate metric depth for the reference view, aligned with the ground-truth extrinsics. We then warp the reference RGB and depth into the target view using the GT camera pose, yielding the final input conditionings for the model.

CAT3D[†]. As the official implementation of CAT3D is not publicly available, we denote by CAT3D[†] a reproduction using the model architecture and checkpoint from CAMEO [22].

C Additional Results

C.1 Evaluation with VGGT Backbone

While our primary evaluation established the effectiveness of the Geometric Latent Diffusion (GLD) framework using Depth Anything 3 (DA3) [26] as the

underlying backbone, we further validate that our core hypothesis generalizes beyond a single specific architecture by evaluating GLD with an alternative geometric foundation model, VGGT [47].

Similar to DA3, VGGT extracts feature representations that are deeply grounded in 3D geometry and multi-view consistency. In this experiment, we replace the DA3 encoder and decoder with those of VGGT, repurposing its intermediate feature space as the latent space for our multi-view diffusion model. The diffusion models are trained from scratch following the exact same configuration and objective described in Appendix A.

As illustrated in Tab. 13 and Fig. 9, although GLD with the VGGT backbone exhibits slightly lower overall performance compared to the DA3 backbone, it consistently outperforms the VAE and DINO baselines. This performance gap is particularly pronounced in 3D evaluation metrics, where the VGGT backbone demonstrates strong geometric consistency and significantly lower pose estimation errors (*e.g.*, ATE) across multiple datasets. These findings confirm that operating within a geometric latent space inherently provides the essential multi-view correspondences and 3D structural priors required for robust novel view synthesis, independent of the specific geometric foundation model architecture.

C.2 Comparison with Method Trained from Scratch

In the main manuscript, we show that our method remains competitive with, and in some cases outperforms, state-of-the-art novel view synthesis (NVS) baselines that leverage large-scale text-to-image (T2I) pretraining. To provide a more controlled and fair comparison, we additionally consider a baseline trained from scratch without any pretrained T2I prior.

Among the baselines included in our study, MVGenMaster [4] is the only method with publicly available training code. We therefore train MVGenMaster from scratch using the same training setup as our method, enabling a controlled comparison that removes the advantage of large-scale generative pretraining.

We compare the methods on the Mip-NeRF 360 [3] dataset, which lies outside our training domain and remains challenging for GLD. As shown in Tab. 14, MVGenMaster trained from scratch performs substantially worse than both its finetuned version and GLD. We attribute this gap to its limited robustness to misalignment between depth and camera parameters, which can induce warping errors during generation. In contrast, the finetuned MVGenMaster benefits from stronger image priors inherited from text-to-image pretraining, making it more tolerant to such errors.

C.3 Additional Qualitative Results

We present additional qualitative results for novel view synthesis using 1, 2, and 4 source views in Fig. 10, Fig. 11, and Fig. 12, respectively. We compare our method with the VAE and DINO baselines across all settings. As shown in the figures, our method consistently produces multi-view results that are more 3D

Table 14: Quantitative comparison of MVGenMaster [4] trained from scratch and GLD (Ours) on out-of-domain [3] datasets.

Methods	From Scratch	2D Metrics			3D Metrics				
		PSNR \uparrow	SSIM \uparrow	LPIPS \downarrow	ATE \downarrow	RPE _r \downarrow	RPE _t \downarrow	Reproj \downarrow	MEt3R \downarrow
Mip-NeRF 360 [3] (Out-of-domain)									
MVGenMaster [4]	\times	14.170	0.304	0.511	0.320	10.92	0.587	0.676	0.402
MVGenMaster [4]	\checkmark	11.217	0.197	0.665	1.804	61.291	3.423	0.720	0.479
GLD (Ours)	\checkmark	14.542	0.288	0.504	0.589	15.97	1.071	0.630	0.406

consistent and photorealistic than those of the baselines, while better preserving geometric structure and appearance across viewpoints.

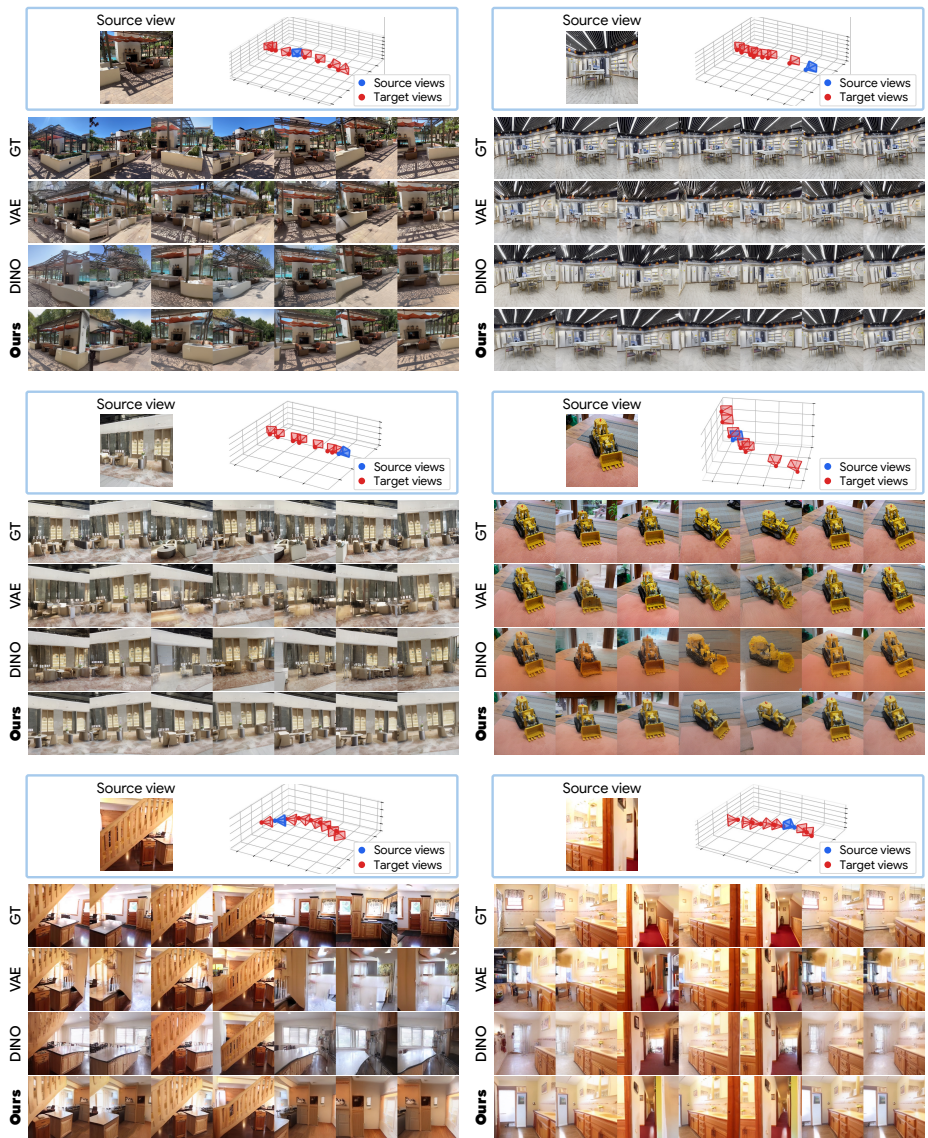


Fig. 10: Additional qualitative results from *one* source views.

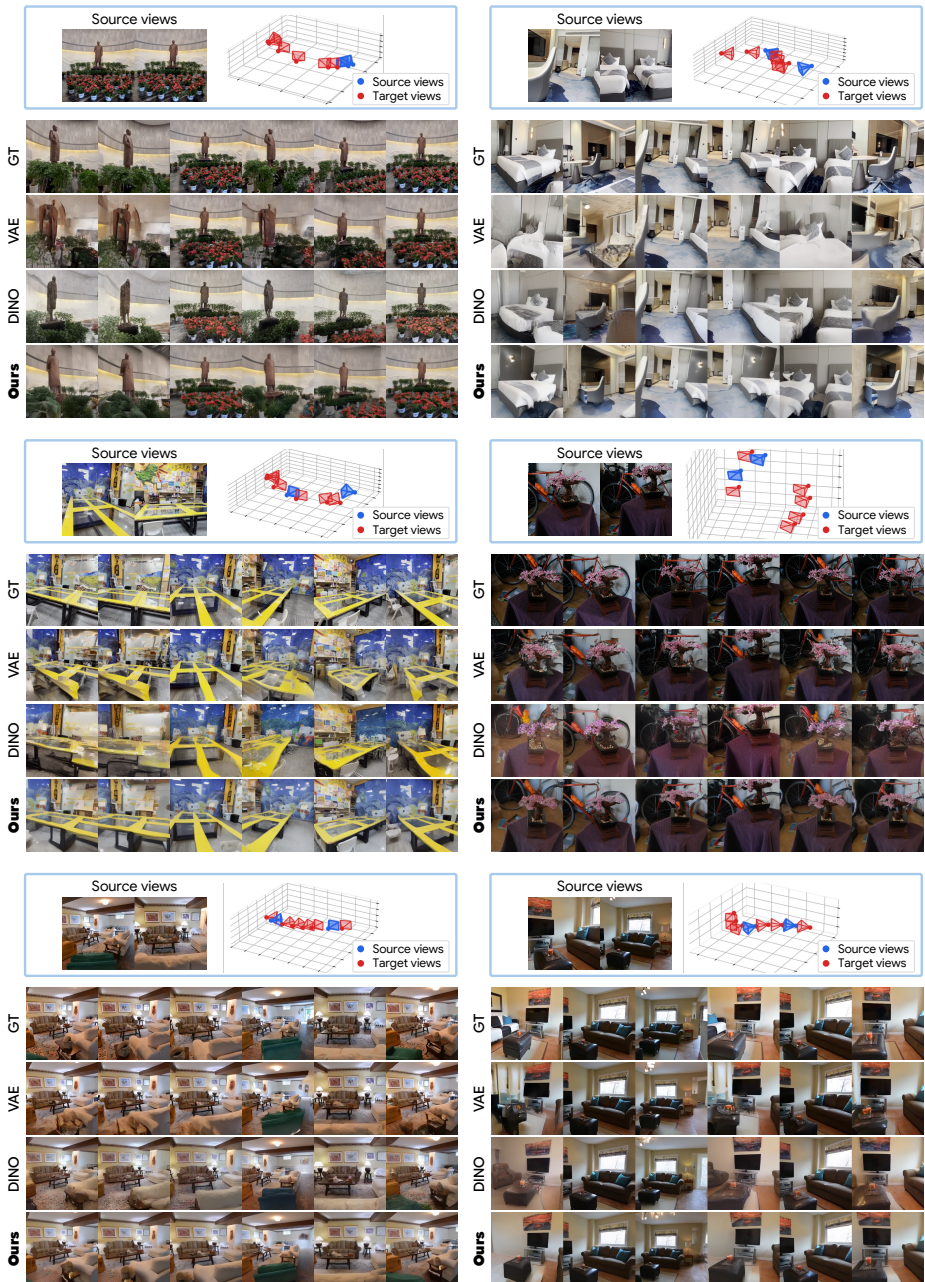


Fig. 11: Additional qualitative results from *two* source views.

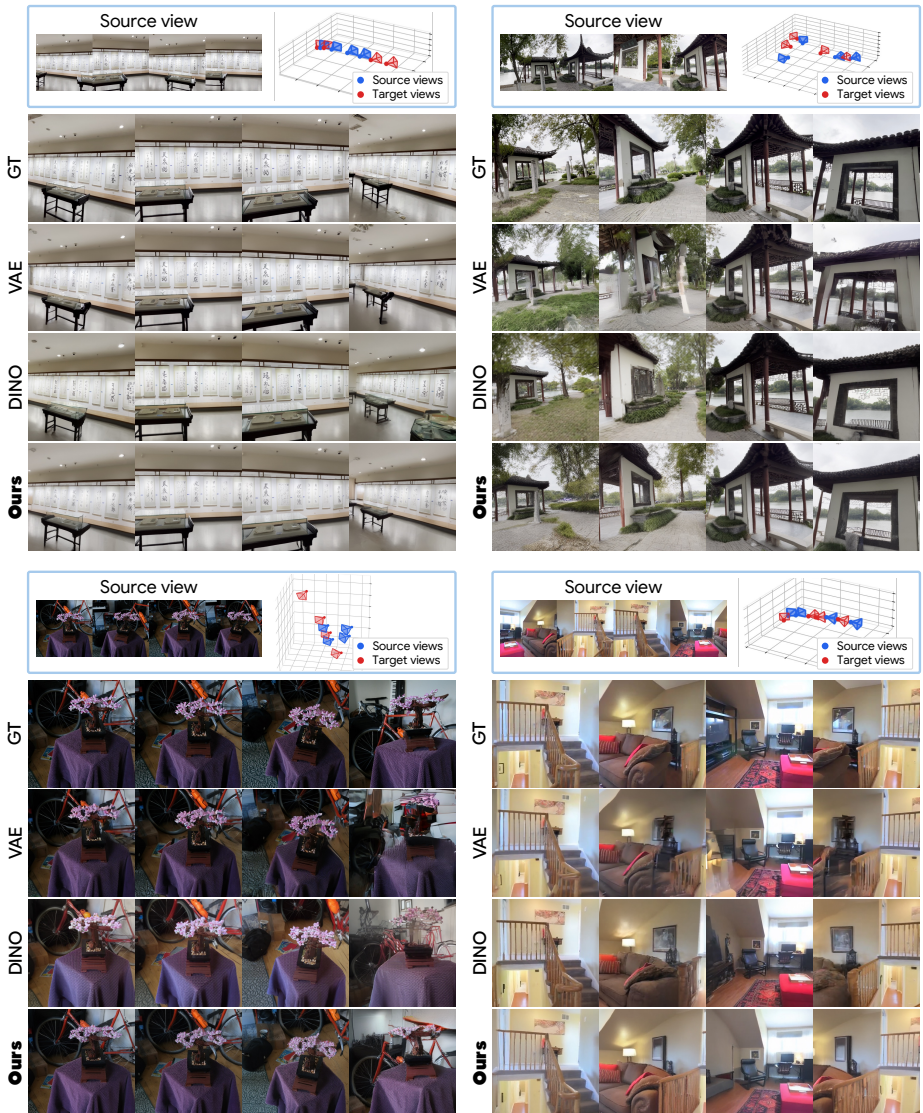


Fig. 12: Additional qualitative results from *four* source views.

C.4 Additional 3D Visualizations

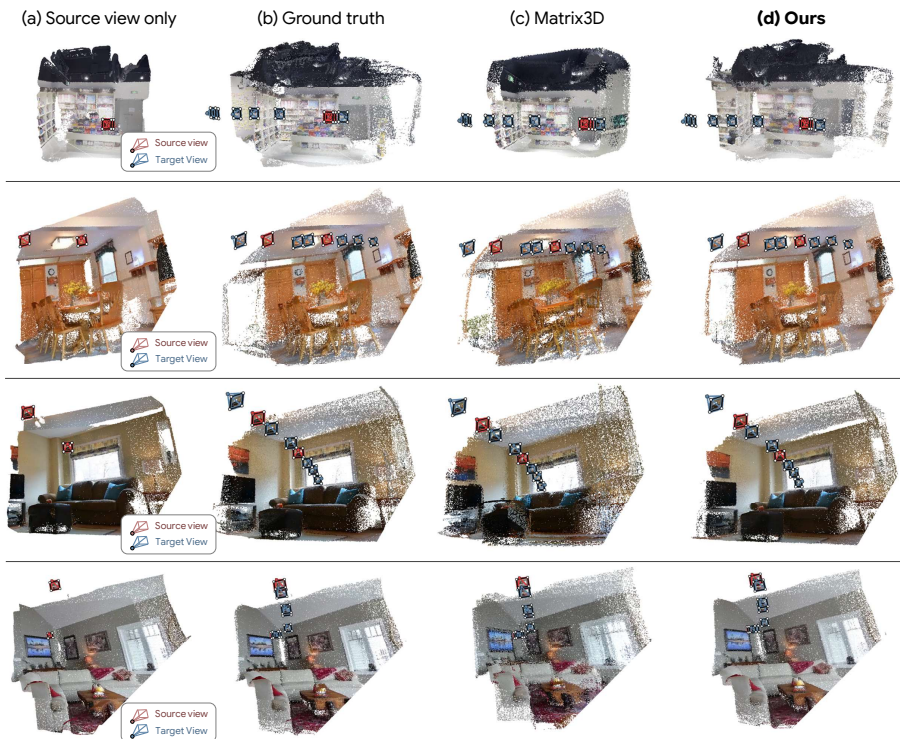


Fig. 13: Additional 3D Visualizations. 3D reconstruction comparisons between Matrix3D and our method. **(b) Ground truth** is reconstructed using DA3 on GT RGB images. Our method yields significantly more consistent and geometrically accurate results.

In Fig. 13, we present additional 3D visualizations comparing our method against Matrix3D. Due to the absence of ground-truth depth data, the reference reconstructions, denoted as ground truth, are generated by processing the ground-truth RGB images with DA3. As illustrated in these results, our approach can produce consistent and geometrically accurate 3D reconstructions.

Specifically, in extrapolative settings where the model synthesizes unobserved regions (rows 1–3), Matrix3D often exhibits misalignment between the newly generated content and the existing source views. For instance, in the dining room scene (row 2), inadequate cross-view consistency in Matrix3D results in a duplicated clock on the wall and blurry chairs. Similarly, in the third row, the generated unseen regions, such as the TV and picture frames on the left wall, do not align properly with the previously observed regions, leading to structural discontinuities. In contrast, our method generates these unobserved areas while maintaining robust 3D consistency. Furthermore, in the interpolative

setting (row 4), our method synthesizes precise viewpoints and RGB-D maps that accurately correspond with the source views, preserving rigid structures and object boundaries without noticeable misalignment artifacts.

D Additional Discussion

D.1 Analysis of Geometric Correspondences in Diffusion Features

CAMEO [22] shows that cross-view correspondence in internal attention maps is a strong indicator of multi-view generation quality, and that models exhibiting stronger correspondence on their 3D attention maps tend to produce more geometrically consistent outputs. To examine whether this relationship holds across different latent spaces, we measure cross-view correspondence of the 3D attention maps at each layer for diffusion models trained in the DA3, VAE, and DINO latent spaces.

Specifically, given an image pair $(\mathcal{I}_1, \mathcal{I}_2)$, we extract the query Q_1^l and key K_2^l from the 3D attention module at each layer l , following CAMEO [22]. Correspondences are estimated by matching each query descriptor in Q_1^l to its nearest neighbor in K_2^l using cosine distance. We evaluate the resulting correspondences on ScanNet [5] using PCK, following the protocol of Probe3D [10]. We report results for \mathcal{M}_1 trained in the DA3 latent space. The results are shown in Fig. 14.

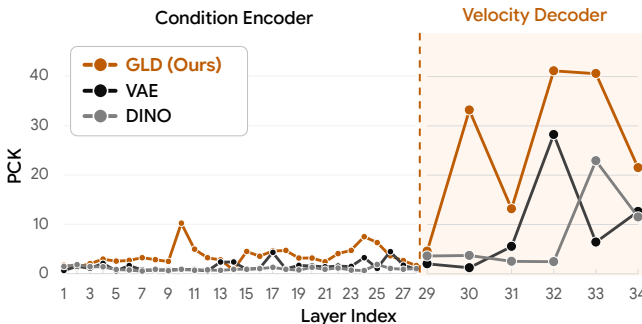


Fig. 14: Geometric correspondence of trained multi-view diffusion models.

Among the three latent spaces, the model trained in the DA3 latent space exhibits the strongest cross-view correspondence across nearly all layers, with the largest margin appearing in the decoder blocks. This is consistent with CAMEO’s finding [22] that stronger internal correspondence correlates with higher-quality multi-view generation, corroborating the superior geometric consistency observed in the final outputs (Tab. 3). Furthermore, this suggests that the DA3 latent space provides a representation that facilitates the diffusion model’s learning of cross-view correspondence, rather than merely enabling better decoding after generation.



Fig. 15: Failure cases.

We also observe a clear asymmetry between the conditional encoder and velocity decoder. Across all three latent spaces, correspondence is essentially absent throughout the condition encoder and emerges only in the velocity decoder, where it increases sharply and peaks at intermediate blocks (layers 31–32). This suggests that the encoder primarily preserves per-view conditioning information, while cross-view geometric correspondence is established in the decoder through 3D attention.

D.2 Computational Cost

We report the sampling time of each model in Tab. 15(A). The model operating in the VAE latent space achieves the fastest generation speed due to its smaller token count, whereas GLD is the slowest because it requires two sampling stages to obtain the complete feature set. We further provide a latency breakdown of each module in GLD in Tab. 15(B). The results show that obtaining level 2 and level 3 features via propagation is more efficient than generating them independently, supporting our design choice to avoid explicit generation of deeper feature levels.

Table 15: Inference latency. Measured on a single RealEstate10K24 [58] scene.

(A) Overall comparison

Method	Sampling (s)	Decode (s)
DINO	35.2	0.41
VAE	28.0	0.50
GLD (ours)	66.1	0.43

(B) GLD runtime breakdown

Phase	Time (s)
Lv.1 sampling	37.8
Lv.1 \rightarrow Lv.2, Lv.3 prop.	0.15
Lv.1 \rightarrow Lv.0 sampling	28.4
RGB decoding	0.43
Total	66.8

D.3 Limitations

While Geometric Latent Diffusion (GLD) demonstrates robust multi-view consistency, a few challenging scenarios remain, as illustrated in Fig. 15. Specifically, in cases of severe occlusion or very sparse spatial coverage, the model may hallucinate content or produce artifacts in regions entirely unobserved by the reference views. Additionally, extreme lighting changes or large temporal gaps between the reference and target inputs can make it difficult to establish reliable cross-view correspondences.